

Signatures of Obliquity in Thermal Phase Curves of Hot Jupiters

ARTHUR D. ADAMS,¹ SARAH MILLHOLLAND,¹ AND GREGORY LAUGHLIN¹

¹*Department of Astronomy, Yale University, New Haven, CT 06520*

ABSTRACT

Recent work suggests that certain short-period transiting extrasolar planets may be trapped in secular spin-orbit resonances, in which the planetary spin precession frequencies match the frequencies of orbital nodal regression (or strong Fourier components thereof). In some of these cases, the transiting planet is expected to have significant spin obliquity with respect to the orbital plane. We employ a thermal radiative model to explore how large polar tilts affect full-phase light curves, and discuss the potentially observable signatures that are expected to result. We show that well-studied short-period planets HD 149026 b and WASP 12 b exhibit light-curve features that may arise from being in high-obliquity states.

Keywords: methods: data analysis, methods: numerical, planets and satellites: atmospheres, planets and satellites: dynamical evolution and stability, planets and satellites: individual (HD 149026 b), techniques: photometric

1. INTRODUCTION

Analysis of the full-phase photometry of transiting extrasolar planets has generated a number of insights. By tracking the emission and the reflection of light from planets as they trace through their orbits, one elicits important clues regarding atmospheric compositions, surface flow patterns, atmospheric thermal responses, cloud coverage, the efficiency of day-to-night heat redistribution and more. Relatively high signal-to-noise detections of full-phase photometry have now been routinely made in both the optical and in the near-infrared, and the technique has been employed as a method of both detection and characterization.

Many short-period planets have been subject to strong tidal evolution which has demonstrably led to complete or near-complete orbital circularization for planets with periods $P \lesssim 5$ d (Rodríguez & Ferraz-Mello 2010). Moreover, because time scales for planetary tidal spin evolution are generally shorter than for orbital evolution, it is usually assumed that short-period planets have zero obliquity, and are spinning synchronously (for orbits with $e = 0$, see e.g. Gladman et al. 1996) or pseudo-synchronously (for orbits with finite eccentricity; see Hut 1981).

Time-resolved photometry of assumed-synchronous planets on circular orbits usually suggests a meteorological situation in which peak infrared emission from the planet lies eastward of the sub-stellar point (e.g. Knutson et al. 2007, 2009a; Cowan & Agol 2011; Knut-

son et al. 2012; Cowan et al. 2012b; Zellem et al. 2014; Schwartz et al. 2017; Zhang et al. 2018). By contrast, phase curves in the optical tend to suggest that peak reflectivity often occurs to the west of the sub-stellar point, and closer to the morning terminator (Shporer 2017). These observations are generally interpreted to imply eastward circumplanetary flow and cloud decks that burn off when advected into the direct beam of installation.

Aspects of this composite picture can be tested when the phase curves of eccentric orbits are tracked (Laughlin et al. 2009)(+Adams, Boos & Wolf 2018). A planet advancing on a non-circular orbit cannot be fully tidally de-spun, and so the surface flows must be dynamically responsive. Bulk properties of the atmosphere such as the radiative response timescale can thus be directly inferred (e.g. Cowan et al. 2012b; de Wit et al. 2016; Adams & Laughlin 2018).

Significant work has been done to develop a mathematical formalism to predict observable effects of the relationship between a planet’s spin, its orbit, and the viewing geometry. Kawahara & Fujii (2010) set up a geometric framework for mapping planets in reflected/scattered light, including for oblique planets, recovering a test model with Earth-like topography and axial tilt. This framework was then extended to account for effects such as cloud cover (Kawahara & Fujii 2011) and generally inclined orbits (Fujii & Kawahara 2012), and signatures of obliquity have been predicted in Fourier analyses of photometry for directly-imaged

planets (Kawahara 2016). Schwartz et al. (2016) demonstrate the ability to infer spin axis orientation for general albedo maps, and set a feasible minimum observing baseline for making robust inferences of the spin axis orientation. Most recently, Farr et al. (2018) present *exocartographer*¹, a software package which generates reflected light photometry for an arbitrary albedo map and spin geometry, and can fit to a variety of time sampling of data.

Our work considers a similar geometric framework in the near-infrared, where the thermal emission from the planet, rather than reflected light from the host star, should be the primary source of the observed flux. Cowan et al. (2012b) considered the effects of eccentricity and obliquity for the phase photometry of an Earth-like planet, and demonstrated that one can infer the characteristic thermal time scales from observations. They also concluded that a combination of optical and infrared observations would be necessary to accurately measure bulk atmospheric conditions, with optical phase curves constraining both the rate and orientation of the planet’s spin, as described above. However, the effects of the spin and orbit will both drive the global-scale heating, and so in principle phase photometry will be sensitive to the combined geometry.

While one can model thermal variations for any choice of orbital shape and spin orientation, we should restrict ourselves to only the scenarios which are physically feasible for systems with close-in giant planets. Conversely, if we infer a particular spin-orbit geometry from observed variations, that will put constraints on the system architecture, which in turn will have dynamical predictions that may be observable.

HD 149026 b is a planet on a 2.88-day orbit which is slightly more massive ($0.38 M_J$), but smaller in size ($0.74 R_J$), than Saturn (Stassun et al. 2017). Its formation is still a matter of ongoing study, given that its density is quite high compared with other giant planets on close-in orbits. Sato et al. (2005) were the first to measure the planet’s radius via transit photometry, and proposed a high core mass of $\approx 67 M_\oplus$ could explain the measurements. Subsequent works have inferred similarly high core masses in the range of $\sim 50\text{--}110 M_\oplus$ (Fortney et al. 2006; Ikoma et al. 2006; Broeg & Wuchterl 2007; Burrows et al. 2007) from combinations of atmospheric and interior modeling. Ikoma et al. (2006) propose that HD 149026 b’s combination of high metallicity and modest H/He envelope can either be explained via planetesimal capture and a limited gas supply, if its current state

was obtained prior to disk dissipation, or a combination of envelope photoevaporation, Roche lobe overflow, and major collisions after disk dissipation.

WASP-12 b is another giant planet in a very short orbit around its host star, but which is known to be tidally distorted due to its density and proximity to its host star (Li et al. 2010; Lai et al. 2010). There is also spectroscopic evidence for extensive diffuse gas beyond the planet’s Roche lobe (Fossati et al. 2010; Haswell et al. 2012; Fossati et al. 2013), as well as hydrodynamic simulations (Debrecht et al. 2018), suggesting significant atmospheric mass loss. Extensive transit observations have been made (detailed further in §2), whose non-constant ephemerides have pointed to either apsidal precession of an eccentric orbit or orbital decay (Maciejewski et al. 2016). Bailey & Goodman (2018) have recently published observations consistent with an in-spiral, which point to a potential third body in the system that can sustain a slight eccentricity in WASP-12 b’s orbit.

Both planets are relatively dense, have no known planetary neighbors (transiting or otherwise), and would require a special dynamical state to be anything other than orbitally circularized, spin synchronized, and with zero obliquity. However, a type of dynamical state known as a Cassini state (Colombo 1966; Peale 1969; Ward 1975), which is driven by a mutual resonance between a known inner planet and a potential non-transiting outer planet, can effect a quasi-stable state where an inner planet can maintain a non-circular orbit, non-synchronous spin, and/or non-zero obliquity. Cassini states have been invoked to explain, for example, the relatively large obliquity of Saturn (Ward & Hamilton 2004; Hamilton & Ward 2004), the spin state of Mercury (Peale 2006), and has been considered as a mechanism to inflate the radii of Hot Jupiters, albeit with disputed feasibility (Levrard et al. 2007; Fabrycky et al. 2007).

In §2 we review the near-infrared photometric observations for HD 149026 b and WASP-12 b, including the analyses of light curve morphologies. §3 details our numerical simulations of known Kepler multi-planet systems which have been perturbed in some way, to make a broad assessment of whether compact multi-planet systems may evolve to states of high mutual inclinations. §4 gives a dynamical analysis with particular focus on application to the HD 149026 system, exploring the possibility that a Cassini state may exist between HD 149026 b and an as of yet undiscovered, non-transiting companion. §5 describes the thermal model, which accounts for a general rotation rate and spin axis orientation. This framework is then employed in §6 to re-analyze the

¹ <https://github.com/bfarr/exocartographer>

Spitzer phase photometry for HD 149026 b and WASP-12 b.

2. PHOTOMETRY

HD 149026 b has been observed in transit in Strömgren b and y (Sato et al. 2005; Winn et al. 2008), g and r (Charbonneau et al. 2006), NICMOS (1.1–2.0 μm) on the Hubble Space Telescope (Carter et al. 2009), and in the 8.0 μm channel of the Infrared Array Camera (IRAC) on the Spitzer Space Telescope (Nutzman et al. 2009). Secondary eclipses have also been observed in each of the 4 IRAC channels (3.6–8.0 μm) and the Infrared Spectrograph (IRS) at 16 μm (Stevenson et al. 2012). Knutson et al. (2009b) presented the first phase photometry, with a phase curve spanning just over half the orbit in 8.0 μm ; most recently Zhang et al. (2018) have published two full-phase observations in the Warm Spitzer bands (3.6 and 4.5 μm). We draw attention to §4.1 of Zhang et al. (2018), where the authors point out inconsistencies between the bands with respect to the phase curves warrant a fair degree of skepticism. In particular, the positive phase offset, or late minimum, of the 3.6 μm , is difficult to explain with a combination of atmospheric modeling with the assumption of spin-orbit synchronization.

WASP-12 b was first discovered in transit via the SuperWASP camera (Hebb et al. 2009), and subsequent transits have been observed in the V band (Chan et al. 2012), R (Maciejewski et al. 2011), J , H , and K_s (Croll et al. 2011), and at 3.6–8.0 μm from Spitzer (Campo et al. 2011; Cowan et al. 2012a; Stevenson et al. 2014). Mandell et al. (2013) have also provided transit spectroscopy from WFC3 (1.1–1.7 μm) on the Hubble Space Telescope. Our work focuses on re-analyzing the full-orbit phase curves available from the warm Spitzer (3.6 and 4.5 μm) channels, originally published in Cowan et al. (2012a).

3. DYNAMICAL EVOLUTION OF A TIGHTLY PACKED SYSTEM

In order to test the feasibility of evolving a dynamically full, multi-planet system into a state broadly consistent with high obliquity, we run dynamical simulations using the REBOUND² software package (Rein & Liu 2012; Rein & Spiegel 2015). We adopt the current orbital configuration and transit parameters of Kepler-107, a known multi-planet system (Rowe et al. 2014; Van Eylen & Albrecht 2015), and explore the statistical distribution of the planetary orbits in the presence of an instability. For each set of runs we perform 100 separate

simulations of maximum 10^6 Earth years each; for both systems this corresponds to $\sim 10^8$ orbits of the innermost planet.

Since the orbital geometry of each of the known planets in Kepler-107 is not entirely constrained by the measured transit parameters from Rowe et al. (2014), we use the following process to randomly generate configurations consistent with these parameters:

1. Set the line of sight to the positive x -axis, the default reference direction in REBOUND³.
2. Choose a longitude of periastron ϖ randomly from a uniform distribution $U(0, 2\pi)$ in radians.
3. Choose a longitude of ascending node Ω from a uniform distribution over the set of angles satisfying

$$|\sin \Omega| \geq b \left[\frac{R_\star + R_P}{r_{\text{tr}}(e, \varpi)} \right] \quad (1)$$

where b is the impact parameter, R_\star and R_P the stellar and planetary radii, respectively, and

$$r_{\text{tr}} \equiv a \left(\frac{1 - e^2}{1 + e \sin \varpi} \right) \quad (2)$$

the star-planet separation at the transit mid-point.

4. Calculate the inclination (in the range $[0, \pi/2]$) that solves the transit condition

$$\sin i |\sin \Omega| = b \left[\frac{R_\star + R_P}{r_{\text{tr}}(e, \varpi)} \right]. \quad (3)$$

After running the simulations for 10^6 years, we evaluate the transit conditions along the initial line of sight for the final orbits of the remaining planets. Figure 1 shows the resulting distributions of these inclinations. In a significant fraction of the outer planets (c – e), the planets no longer transit, with inclinations reaching 30–40°. (ACTUAL RESULTS ARE STILL TO COME FROM THE STILL-RUNNING MODELS, AND THESE NUMBERS WILL ALMOST CERTAINLY CHANGE.) In half of the nominal runs, and all but one of the inner-Jupiter runs, the outermost planet e is ejected from the system, which we define as reaching an orbital semi-major axis one order of magnitude larger than its initial value.

³ Note that in this setup, an inclination of zero will imply the orbit is viewed edge-on, rather than the standard $i = 90^\circ$. We adopt this non-standard definition purely for convenience.

² <https://github.com/hannorein/rebound>

Table 1. Orbital and Transit Properties for Kepler-107

Planet	P (yr)	a (AU)	e	M_p (M_J)	R_p (R_J)	b	T_{tran} (BJD $- 2454900$)
b	$3.179997 \pm 1.1 \times 10^{-5}$	0.044	$0.020^{+0.200}_{-0.020}$	0.01167	0.139 ± 0.005	0.34 ± 0.24	66.49904 ± 0.00200
c	$4.901425 \pm 1.6 \times 10^{-5}$	0.059	$0.020^{+0.260}_{-0.020}$	0.0133	0.161 ± 0.016	0.78 ± 0.29	71.60742 ± 0.00174
d	$7.958203 \pm 1.04 \times 10^{-4}$	0.082	$0.14^{+0.25}_{-0.14}$	0.00371	0.095 ± 0.005	0.27 ± 0.24	70.79968 ± 0.00612
e	$14.749049 \pm 3.4 \times 10^{-5}$	0.123	$0.020^{+0.180}_{-0.020}$	0.0360	0.308 ± 0.022	0.90 ± 0.28	71.77998 ± 0.00134

References—Orbital eccentricities are taken from [Van Eylen & Albrecht \(2015\)](#). The masses are calculated from an empirical relation calculated on [exoplanets.org](#), detailed in [Han et al. \(2014\)](#). All other values are from [Rowe et al. \(2014\)](#).

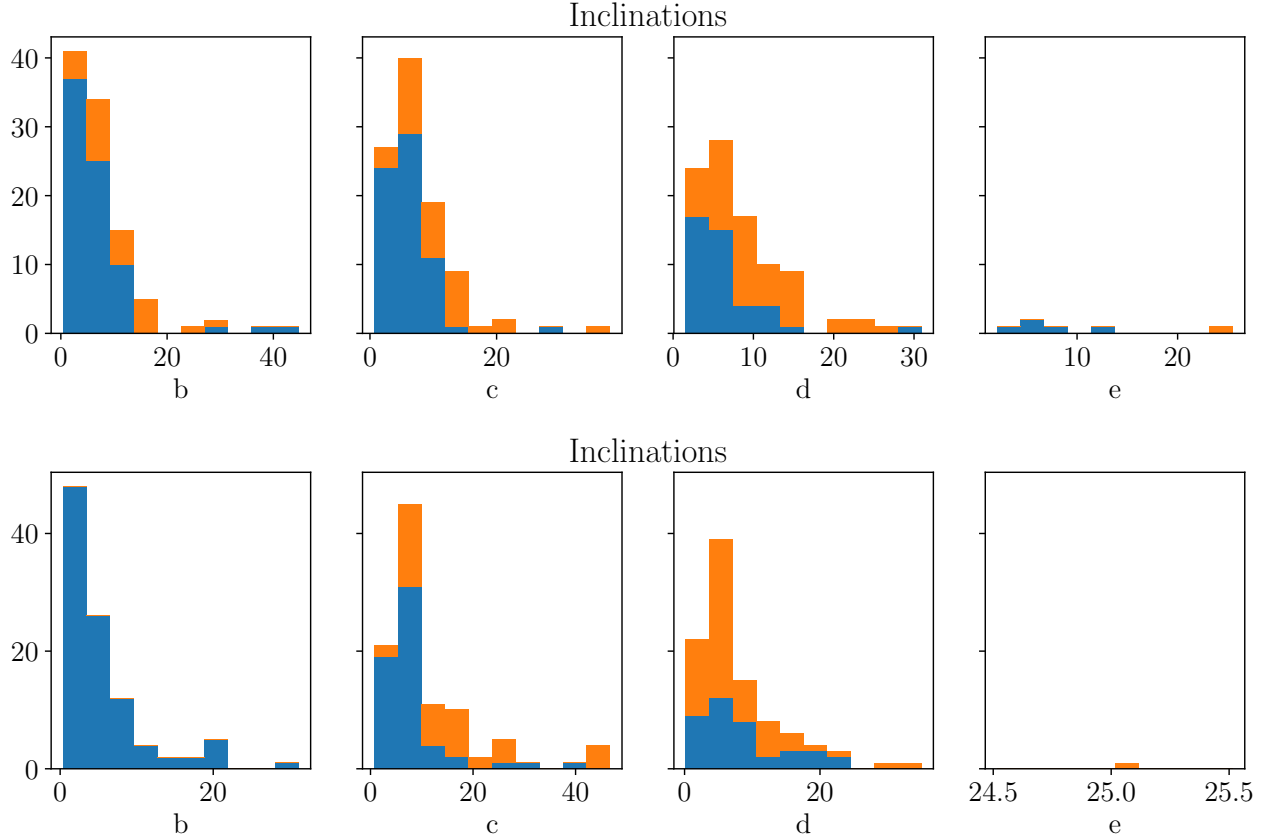


Figure 1. *Top:* the distribution of mutual inclinations (in degrees) from the net angular momentum vector, for the nominal Kepler-107 system randomized over orbital parameters consistent with the observed transit parameters. *Bottom:* the same distributions where the mass of planet b is increased from $3.7 M_{\oplus}$ to that of Jupiter. Blue entries denote planets which still transit according to all the calculated orbital parameters. Orange entries denote those that will not transit.

4. CASSINI STATE DRIVEN BY AN INCLINED, EXTERNAL PERTURBER

Tidal torques, which are strongest for close-in and large-radius planets like HD 149026 b , act to dampen planetary obliquities to zero. Large obliquities can be maintained, however, if a planet is locked in a secular spin-orbit resonance called a Cassini state ([Colombo 1966](#); [Peale 1969](#); [Ward 1975](#)). In this configuration, the

planet’s spin and orbital axes precess at the same rate about the same axis. The three axes are coplanar in a dissipation-less Cassini state, but the spin axis is shifted out of the plane in the presence of tides.

In this section, we consider the scenario that HD 149026 b has its spin axis trapped in a high obliquity Cassini state as a result of a spin-orbit resonance with an exterior perturber. We begin by calculating the fre-

quencies of spin and orbital precession and then examine the constraints imposed on the hypothetical perturbing planet in order for the scenario to be plausible.

4.1. Spin-orbit resonant frequencies

The torque from the host star on a rotationally-flattened planet will cause the planet's spin-axis to precess about the orbit normal at a period, $T_\alpha = 2\pi/(\alpha \cos \epsilon)$. Here ϵ is the obliquity and α is the precession constant (Ward & Hamilton 2004), which, in the absence of satellites, is given by

$$\alpha = \frac{1}{2} \frac{M_\star}{m_p} \left(\frac{R_p}{a} \right)^3 \frac{k_2}{C} \omega, \quad (4)$$

where we've used m_p , the planet mass, C , the moment of inertia normalized by $m_p R_p^2$, and the spin frequency, ω . We have assumed that J_2 , the coefficient of the quadrupole moment of the planet's gravitational field, takes the form (Ragozzine & Wolf 2009),

$$J_2 = \frac{\omega^2 R_p^3}{3Gm_p} k_2. \quad (5)$$

To estimate the spin-axis precession period of planet "b", we adopted the following parameters: $M_\star = 1.345 M_\odot$, $m_p = 0.36 M_{\text{Jup}}$, $R_p = 0.725 R_{\text{Jup}}$, $a = 0.042$ au, $k_2 = 0.1$ (Kramm et al. 2011), $C = 0.2$, and $P_{\text{rot}} = 2P = 5.75$ days. This results in an estimate, $T_\alpha \cos \epsilon = 2\pi/\alpha \approx 30$ years.

The secular spin-orbit resonance requires a commensurability between the planet's spin-axis precession frequency and its orbit nodal regression frequency, $g = \dot{\Omega}$. In a two-planet system, the nodes of both planets regress uniformly due to secular perturbations. The frequency is given by Laplace-Lagrange theory to be

$$g_{\text{LL}} = -\frac{1}{4} b_{3/2}^{(1)}(\alpha_{12}) \alpha_{12} \left(n_1 \frac{m_2}{M_\star + m_1} \alpha_{12} + n_2 \frac{m_1}{M_\star + m_2} \right) \quad (6)$$

if the planets are not near mean-motion resonance (Murray & Dermott 1999). Here, $\alpha_{12} = a_1/a_2$ and n_i is the mean-motion of planet i , $n_i^2 = GM_\star/a_i^3$. The constant, $b_{3/2}^{(1)}(\alpha_{12})$ is a Laplace coefficient, defined by

$$b_{3/2}^{(1)}(\alpha_{12}) = \frac{1}{\pi} \int_0^{2\pi} \frac{\cos \psi}{(1 - 2\alpha \cos \psi + \alpha^2)^{3/2}} d\psi. \quad (7)$$

In addition to planet-planet interactions, the stellar quadrupole gravitational moment also induces orbit nodal recession about the stellar spin vector, which, in the absence of secular planet interactions, occurs at the frequency

$$g = n \frac{k_2}{2} \left(\frac{\omega_\star}{n} \right)^2 \left(\frac{R_\star}{a} \right)^5. \quad (8)$$

In a multiple-planet system then, the planets orbit normal vectors are perturbed by two components at different frequencies. One frequency, g_\star , is associated with the large oblateness-induced stellar quadrupole moment and the other, g_{p-p} , is due to the planet-planet perturbations. These are close but not exactly equal to the equations 6 and 8 above, since the analytical expressions only account for one driver of nodal regression at a time.

4.2. Constraints on m_2 and a_2 of an inclined companion

Suppose that planet "b" is in a high obliquity spin-orbit resonance with its orbital precession induced by secular interactions with an exterior, inclined, and as-yet undetected companion. There exist limits on the companion's mass, semi-major axis, and inclination in order for this scenario to be feasible. These constraints stem from upholding the Cassini state, preserving total angular momentum conservation, and maintaining consistency with existing radial velocity data. The constraints are outlined in more detail in the sections below.

4.2.1. Constraints from maintaining the Cassini state

If planet "b" is captured in a Cassini state, then there will be a resonance (Ward & Hamilton 2004),

$$|g| \approx \alpha \cos \epsilon. \quad (9)$$

Here we've assumed that the planetary obliquity, ϵ , is large compared to the mutual inclination between the orbits. We may use this condition to calculate the zone of m_2/a_2 parameter space allowing for resonant commensurability.

In Figure 2, we show as a function of m_2 and a_2 the obliquity of planet "b" necessary for the resonance to hold. We assume that the nodal regression frequency is the one associated with the planet-planet interaction, $g = g_{p-p} \approx g_{\text{LL}}$. We also assume $e_b = 0$ and that the spin rate of planet "b" is at equilibrium, $\omega = \omega_{\text{eq}}$, where ω_{eq} is given by (Levrard et al. 2007)

$$\omega_{\text{eq}} = n \frac{2 \cos \epsilon}{1 + \cos^2 \epsilon}. \quad (10)$$

Here $n = 2\pi/P$ is the mean-motion. Combining equations 4, 9, and 10, the resonance condition becomes

$$|g| = \alpha_{\text{syn}} \frac{2 \cos^2 \epsilon}{1 + \cos^2 \epsilon}, \quad (11)$$

where α_{syn} is the value of α in the case of synchronous rotation, $\omega = n$. The solution for ϵ is

$$\cos \epsilon = \left(\frac{1}{2\alpha_{\text{syn}}/|g| - 1} \right)^{1/2}. \quad (12)$$

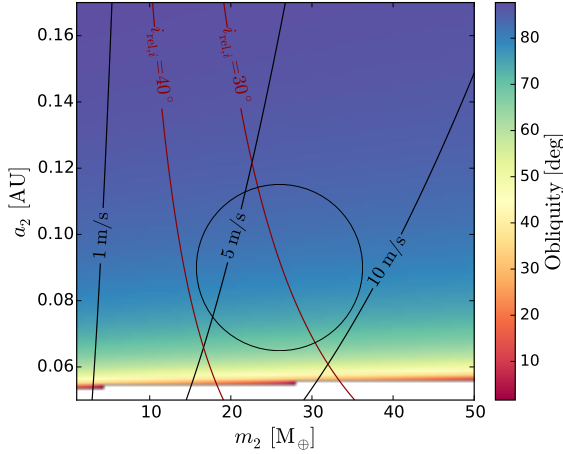


Figure 2. A map of the obliquity that HD 149026 b would have if it was captured in a secular spin-orbit resonance with an external perturber of mass, m_2 , and semi-major axis, a_2 . Contours of radial velocity semi-amplitude are shown in black. Contours of the initial mutual inclination, i_i between the planets at the onset of resonance are shown in red (see section 4.2.2). The permissible region with $i_i \lesssim 40^\circ$ and $K \lesssim 5 - 10$ m/s is indicated with arrows.

Figure 2 shows that if a_2 is too small, $|g|$ is too large and no resonance is possible (white region). Alternatively, if a_2 is too large, $|g|$ is small and $\epsilon \sim 90^\circ$, which is not long-term sustainable. The outer planet is therefore constrained to $a_2 \sim 0.06 - 0.15$ AU.

4.2.2. Constraints from angular momentum conservation

The rate at which tides convert orbital energy into heat energy in an oblique planet is orders of magnitude stronger than it would be in the case of zero obliquity (Levrard et al. 2007). If planet “b” has a large obliquity, it is tidally migrating inwards towards the star, decreasing $|g|/\alpha$ in the process and further exciting its obliquity. The decrease in orbital angular momentum must be counteracted such that total angular momentum of the system is conserved. The second planet must have enough angular momentum to absorb this, thereby limiting the range of allowable orbits.

We define ϕ to be the angle between the stellar spin vector and the total orbital angular momentum vector of the two planets combined. In addition, we define i to be the angle between the two planet’s orbital angular momentum vectors. Then, assuming the planets’ own spin angular momenta are negligible, the total angular momentum is given by

$$J^2 = L_\star^2 + L_1^2 + L_2^2 + 2L_1L_2 \cos i + 2L_\star(L_1^2 + L_2^2 + 2L_1L_2 \cos i)^{1/2} \cos \phi. \quad (13)$$

Secular interactions between the planets do not change a_2 or e_2 , so L_2 remains fixed. Therefore, as L_1 decreases, conservation of J must be upheld by an increase in L_\star through tidal spin-up of the star (Brown et al. 2011) or a decrease in i and ϕ through reorientation of the orbits. There are limits on the amount of orbital reorientation that was possible starting from the initial capture into the Cassini state; $i_i \gtrsim 40^\circ$ is unlikely because above this, Kozai-Lidov eccentricity/inclination oscillations would ensue. The limits that this i_i constraint places in m_2/a_2 space depend on the initial semi-major axis of planet “b”, a_{1i} , the final (present-day) mutual inclination, i_f , the initial and final spin-orbit misalignments, ϕ_i and ϕ_f , and the degree of stellar spin-up.

To develop conservative constraints, we first assume L_\star stayed constant. If any amount of stellar spin-up occurred, the constraints imposed by i_i in m_2/a_2 space are substantially less severe. Wolf et al. (2007) measured a modest sky-plane spin-orbit misalignment, $\lambda = -12^\circ \pm 15^\circ$, via Rossiter-McLaughlin measurements. Motivated by these observations, we consider plausible values, $\phi_i = 20^\circ$ and $\phi_f = 10^\circ$. We assume a small present-day mutual inclination, $i_f = 2^\circ$ for reasons described in the next section. (*Also need justification for a_{1i} decision.*)

Using the parameters outlined above, the i_i contours in Figure 2 were calculated such that conservation of Equation 13 was enforced.

4.2.3. Constraints from radial velocity data

Overlaid on Figure 2 are contours of the outer planet’s RV semi-amplitude assuming an edge-on orbit. In reality, the planet’s orbit would be inclined since it is non-transiting; $i \neq 90^\circ$ opens up more parameter space by moving the contours to the right. If it exists, the inclined planet cannot have a large RV semi-amplitude otherwise it would have been detected in the current data.

The Lick-Carnegie Exoplanet Survey Team (LCES) collected 8.5 years of Keck/HIRES Doppler velocity data on the system (Butler et al. 2017). Using this data we may examine the RV residuals and determine the maximum RV semi-amplitude that an as-yet undetected planet could have. Figure 3 shows the Keck RVs phase-folded at the period of planet “b”, $P = 2.87588874$ days. The second panel shows the residuals of a simple fit with zero eccentricity. The x-axis is index (rather than time or phase), in order to better visualize the overall scatter. The standard deviation of the residuals is 6.7 m/s; the residuals indicate that there may exist a second, as-yet undetected planet with RV semi-amplitude $K \lesssim 5 - 10$ m/s.

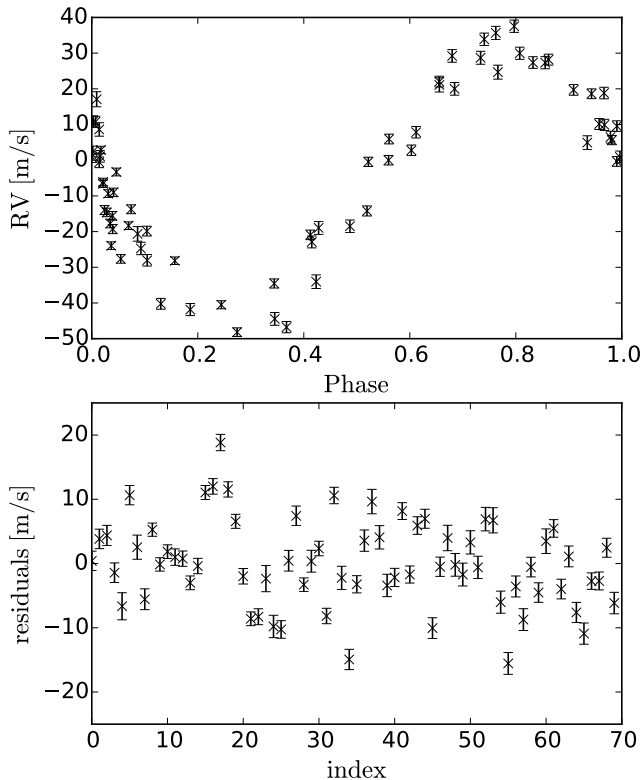


Figure 3. Top panel: Keck/HIRES Doppler velocity measurements of HD 149026 phase-folded at the period of planet b, $P = 2.87588874$ days. Bottom panel: Residuals of a circular orbit fit as a function of index.

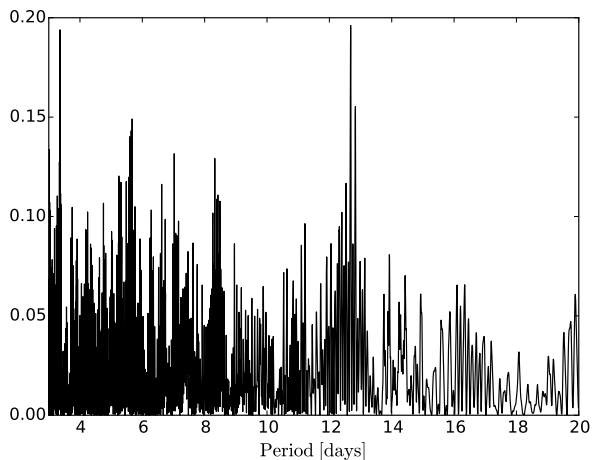


Figure 4. Lomb-Scargle periodogram of the RV residuals.

Figure 4 displays a Lomb-Scargle periodogram of the RV residuals. The highest peak is at 12.68 days. This may be related to stellar activity, since the peak is close to the ~ 13 day stellar rotation period suggested by the $v \sin i$ measurement from Sato et al. (2005). Alternatively, it may be the signature of an additional planet.

In addition to constraining the RV semi-amplitude, the RV data offers more information on the hypothetical planet. Interactions between the mutually-inclined planets produce secular precession that changes the line-of-sight inclination of both of their orbits. The inclination evolution for planet “b” cannot be too large or too fast such that it would have been observable in the 8.5 year baseline of RV data.

4.3. Example simulation of a stable Cassini state

** Here present a simulation of planet b in a stable Cassini state. The mechanism of capture doesn’t matter, but discuss possible capture possibilities. (Planet b would have been closer in.) Also discuss constraints on Q either here or in another section. **

5. COMPONENTS OF THE THERMAL MODEL

We build upon the model framework developed for the analysis in Adams & Laughlin (2018). Each planet is divided into a grid with cells of dimension $5^\circ \times 5^\circ$ by latitude and longitude. There are 6 tunable parameters which all ultimately govern the resulting thermal emission. The first three (the albedo A , equilibrium radiative timescale τ_{rad} , and minimum temperature T_0) most directly parametrize the thermal properties of each cell, and will be put into their formal context in §5.1. In short, each cell absorbs a fraction $1 - A$ of radiation from the host star, and re-radiates as a blackbody with a corresponding characteristic timescale. Its brightness temperature is set both by the time-dependent instellation and any non-stellar heating (e.g. from the planet interior), the latter of which is modeled as keeping the planet at or above a minimum temperature. The remaining three parameters effectively define the components of the rotation vector. Movement of the cells in the model is set entirely by the rotation; the planet rotates with some angular frequency ω_{rot} ($\equiv 2\pi/P_{\text{rot}}$ for the rotation period P_{rot}) with some orientation of its axis (given by two spherical angles ζ and ψ) relative to the orbital plane. The time evolution of grid cell temperatures is convolved with both the viewing geometry from Earth, and the relevant instrumental band profiles, to predict full-orbit light curves for a given set of parameter values. Our fitting routine is detailed in §5.4.

5.1. Thermal Evolution of the Cells

Our planetary model is initialized at apastron with a uniform surface temperature T_0 ; for planets on circular orbits, we set an arbitrary argument of periastron $\varpi = \pi/2$ such that “apastron” occurs during secondary eclipse. To calculate the incoming stellar radiation over the orbit, we start with the star-planet separation

$$r(t) = a \left(\frac{1 - e^2}{1 + e \cos \nu} \right) \quad (14)$$

where a is the orbital semi-major axis, e the orbital eccentricity, and $\nu = \nu(t)$ the true anomaly. To solve for the true anomaly from the time in orbit we first calculate the mean anomaly M , which is directly proportional to time: $M(t) = \omega_{\text{rot}} (t - t_{\text{peri}})$ for rotation rate ω_{rot} and periastron passage time t_{peri} . The eccentric anomaly $E = E(t)$ is then given by Kepler’s equation

$$M(t) = E - e \sin E. \quad (15)$$

There is a direct relation between regular time intervals and regular intervals in mean anomaly, but not for eccentric anomaly (and therefore by extension the true anomaly); we must calculate the latter numerically. Finally, the sine and cosine of the true anomaly may be calculated via

$$\begin{aligned} \cos \nu &= \frac{\cos E - e}{1 - e \cos E} \\ \sin \nu &= \frac{\sqrt{1 - e^2} \sin E}{1 - e \cos E \cos E}. \end{aligned} \quad (16)$$

At each time t in the orbit and longitude/latitude (ϕ, θ) on the planetary surface the equilibrium temperature is calculated via

$$T_{\text{eq}}^4(\phi, \theta, t) = (1 - A) \left(\frac{L_\star}{4\pi\sigma r^2} \right) \cos \alpha_\star + T_0^4 \quad (17)$$

where A is the planetary albedo, L_\star the stellar luminosity, σ the Stefan-Boltzmann constant, $r = r(t)$ the previously calculated star-planet separation, $\alpha_\star = \alpha_\star(\phi, \theta, t)$ the local stellar altitude, and T_0 the minimum temperature parameter. The stellar altitude α_\star is, relative to the sub-stellar point pointed to by $\hat{r}_\star = \phi_\star \hat{\phi} + \theta_\star \hat{\theta}$ and the unit normal \hat{n} at the position,

$$\cos \alpha_\star = \begin{cases} \hat{n} \cdot \hat{r}_\star, & \hat{n} \cdot \hat{r}_\star \geq 0 \\ 0, & \hat{n} \cdot \hat{r}_\star < 0 \end{cases} \quad (18)$$

where $\hat{n} \cdot \hat{r}_\star \rightarrow \hat{r} \cdot \hat{r}_\star = \cos \theta \cos \theta_\star [\cos(\phi - \phi_\star) - 1] + \cos(\theta - \theta_\star)$ for spherical planets, and the sub-stellar point is given by

$$\begin{aligned} \phi_\star &= \phi_\star(t_0) - \left\{ \omega_{\text{rot}} (t - t_0) + \arctan \{ \cos \psi \cot [(\nu - \zeta) - \nu(t_0)] \} \right\} \\ \theta_\star &= \sin^{-1} [\sin \psi \cos(\nu - \zeta)]. \end{aligned} \quad (19)$$

For tidally distorted planets, the unit normal \hat{n} no longer matches the position unit vector \hat{r} ; §5.3 covers this case.

Finally, the change in temperature of each cell in time is calculated as

$$\dot{T}(\phi, \theta, t) = \frac{T_{\text{eq}}}{4\tau_{\text{rad}}} \left\{ 1 - \left[\frac{T(\phi, \theta, t)}{T_{\text{eq}}} \right]^4 \right\} \quad (20)$$

which is a differential equation we can evaluate numerically for sufficiently small timesteps. (The default timestep is 0.5% of the orbital period for circular orbits.)

5.2. Generating Observables

Given a temperature map $T(\phi, \theta, t)$, we solve for the corresponding planet-star flux contrast via

$$\bar{F}(t) = \left(\frac{R_p}{R_\star} \right)^2 \frac{\iiint \lambda w B_\lambda(T) V d\lambda d\theta d\phi}{\iiint \lambda w B_\lambda(T_\star) V d\lambda d\theta d\phi} \quad (21)$$

where $B_\lambda(T)$ is the specific blackbody intensity at a wavelength λ and temperature T , $w = w(\lambda)$ the weighted response of the instrumental bandpass at λ , and $V = V(\phi, \theta, t)$ is the component of the normal vectors of the cells along the line of sight. In the spherical static system this component is

$$V = \begin{cases} \hat{n} \cdot \hat{r}_{\text{obs}}, & \hat{n} \cdot \hat{r}_{\text{obs}} \geq 0 \\ 0, & \hat{n} \cdot \hat{r}_{\text{obs}} < 0 \end{cases} \quad (22)$$

where the sub-observer point is given by

$$\begin{aligned} \phi_{\text{obs}} &= \phi_\star(t_{\text{ecl}}) - \omega_{\text{rot}} (t - t_{\text{ecl}}) \\ \theta_{\text{obs}} &= \sin^{-1} [\sin \psi \cos(\nu_{\text{ecl}} - \zeta)] \end{aligned} \quad (23)$$

and $\nu_{\text{ecl}} = 3\pi/2 - \varpi$ is the true anomaly during secondary eclipse (i.e. at time t_{ecl}), and for spherical planets, $\hat{n} \cdot \hat{r}_{\text{obs}} = \cos \theta \cos \theta_{\text{obs}} [\cos(\phi - \phi_{\text{obs}}) - 1] + \cos(\theta - \theta_{\text{obs}})$. However, as with the stellar altitude, for non-spherical planets the calculation is a bit more complicated (see §5.3).

5.3. A Simple Model of Tidal Distortion

A tidally distorted planet can have a considerably non-spherical shape. We first outlined a model of tidal non-sphericity in Appendix A of Adams & Laughlin (2018). Here we adopt that work’s primary assumption to model the distorted shape as a prolate spheroid, with the long axis displaced clockwise in the orbital plane from the star-planet line by some lag angle $\lambda \equiv \cos^{-1}(\hat{r}_\star \cdot \hat{r}_\ell)$. We will assume this lag angle is zero for our analysis, but include it for completeness. The lengths of the long and short axes are dictated by the gravitational potential of the star-planet system. Consider a coordinate system

where \hat{z} points from the planet center along the long axis, \hat{y} points along the orbit normal, and \hat{x} points along the short axis according to a right-handed coordinate system. Then the potential becomes

$$\begin{aligned} \Phi(\vec{r}) = -\frac{GM_\star}{a} & \left\{ \left[\left(\frac{z}{a} + \frac{\xi}{1+\xi} \right)^2 + \left(\frac{x^2+y^2}{a^2} \right) \right]^{-1/2} \right. \\ & + \left[\left(\frac{z}{a} + \frac{1}{1+\xi} \right)^2 + \left(\frac{x^2+y^2}{a^2} \right) \right]^{-1/2} \\ & \left. + \frac{1+\xi}{2} \left(\frac{x^2+z^2}{a^2} \right) \right\} \end{aligned} \quad (24)$$

where a is the orbital semi-major axis and ξ is the planet-star mass ratio M_p/M_\star . We then fit the cross-sectional area along \hat{x} and \hat{y} to the observed transit depth to get the long and short axis lengths⁴.

For an ellipsoid the area of each cell is position-dependent, and will therefore affect the surface area over which it radiates. Once we have the planetary semi-major and semi-minor extents (defined as one-half of the long and short axes, respectively), denoted A_p and B_p , we can calculate the areas of individual cells. We adapt the result from [Adams & Laughlin \(2018\)](#) (Equation A7) for the area of a cell spanning longitudes ϕ_i – ϕ_j and latitudes θ_i – θ_j , now with a more complicated relationship between the Cartesian coordinates for the planet:

$$\begin{aligned} S_{ij} = B_p^2 \int_{\phi_i}^{\phi_j} \int_{\theta_i}^{\theta_j} \cos \theta & \left\{ 1 \right. \\ & + (\chi^2 - 1) \left[\frac{1}{4} f(\phi, \theta) + 2(\hat{r} \cdot \hat{r}_\ell) \right] \\ & \left. + (\chi^2 - 1)^2 (\hat{r} \cdot \hat{r}_\ell)^2 \right\}^{1/2} d\theta d\phi, \end{aligned} \quad (25)$$

where $\chi \equiv A_p/B_p$ is the axis ratio and

$$\begin{aligned} f(\phi, \theta) = \{ \sin \theta \cos \theta_\ell [\cos(\phi - \phi_\ell) - 1] & - \sin(\theta - \theta_\ell) \}^2 \\ + \cos^2 \theta_\ell [\sin(\phi - \phi_\ell) + 1] \end{aligned} \quad (26)$$

A second effect of the non-spherical shape is a change in the stellar altitude as a function longitude and latitude. To quantify the change we first write the function representing the shape of the prolate ellipsoid:

$$f(x, y, z) = \frac{x^2 + y^2}{B_p^2} + \frac{z^2}{A_p^2}. \quad (27)$$

⁴ In general the solution yields unequal extents along \hat{x} and \hat{y} , while the prolate spheroid assumption implies they are equal. For WASP-12 b, the differences are minor enough that the corresponding differences in calculated ellipticity are $\lesssim 0.01$.

We need a way of expressing these ellipsoidal coordinates in the oblique coordinates (i.e. with respect to the latitude/longitude coordinates defined by the rotation). To do this we note that we can express the oblique positions of both the sub-stellar point, given by Equation 19, and the extreme point of the planet along the long axis, given by

$$\begin{aligned} \phi_\ell &= \phi_\star(\nu \rightarrow \nu - \lambda) \\ \theta_\ell &= \theta_\star(\nu \rightarrow \nu - \lambda) \end{aligned} \quad (28)$$

. If the lag angle $\lambda > 0$, then we can construct our ellipsoidal Cartesian unit vectors entirely with respect to the unit position vectors for these two points:

$$\begin{aligned} \hat{x} &= \frac{\hat{r}_\star - \cos \lambda \hat{r}_\ell}{\sin \lambda} \\ \hat{y} &= \frac{\hat{r}_\ell \times \hat{r}_\star}{\sin \lambda} \\ \hat{z} &= \hat{r}_\ell. \end{aligned} \quad (29)$$

From this the normal unit vector at a given point on the surface is given by

$$\begin{aligned} \hat{n} &= \vec{\nabla} f / \|\vec{\nabla} f\| \\ &= \{1 + g^{-1}[\chi, (\hat{r} \cdot \hat{r}_\ell)]\}^{-1/2} [(\hat{r} \cdot \hat{x}) \hat{x} + (\hat{r} \cdot \hat{y}) \hat{y}] \\ &\quad + \{1 + g[\chi, (\hat{r} \cdot \hat{r}_\ell)]\}^{-1/2} \hat{z} \end{aligned} \quad (30)$$

where

$$g[\chi, (\hat{r} \cdot \hat{r}_\ell)] \equiv \chi^2 \left[\frac{1 - (\hat{r} \cdot \hat{r}_\ell)^2}{(\hat{r} \cdot \hat{r}_\ell)^2} \right] \quad (31)$$

Then the cosines of the stellar altitude and the visibility are given by the component of \hat{n} along the instellation and observer lines, as in Equations 18 and 22.

$$\begin{aligned} \cos \alpha_\ell &= \hat{n} \cdot \hat{r}_\star \\ &= \sin \lambda (1 + g^{-1})^{-1/2} [\hat{r} \cdot \hat{r}_\star - \cos \lambda (\hat{r} \cdot \hat{r}_\ell)] \\ &\quad + \cos \lambda (1 + g)^{-1/2} (\hat{r} \cdot \hat{r}_\ell) \end{aligned} \quad (32)$$

and the component along the observer line is

$$\begin{aligned} V &= \hat{n} \cdot \hat{r}_{\text{obs}} \\ &= \frac{\cos(\nu - \nu_{\text{ecl}}) - \cos[(\nu - \lambda) - \nu_{\text{ecl}}]}{\sin \lambda} (1 + g^{-1})^{-1/2} \\ &\quad \times [\hat{r} \cdot \hat{r}_\star - \cos \lambda (\hat{r} \cdot \hat{r}_\ell)] \\ &\quad + \cos[(\nu - \lambda) - \nu_{\text{ecl}}] (1 + g)^{-1/2} (\hat{r} \cdot \hat{r}_\ell). \end{aligned} \quad (33)$$

5.4. MCMC Optimization

We sample parameter space uniformly over physically feasible ranges in each, and calculate Gaussian likelihoods in each to get a sense of the landscape of likelihoods. An annealing Metropolis-Hastings algorithm allows us to use Markov-Chain Monte Carlo techniques to

rapidly find an optimal likelihood. In order to quantify the uncertainty in the parameters we run new MCMC chains without annealing, starting at points in parameter space corresponding to the best fits, using the 68% ranges of explored values on either side of the best-fit parameter values to define $1\text{-}\sigma$ uncertainties. For the uncertainty ranges in the light curves, we pull the 68% ranges in likelihood for each set of parameters, and plot the range in fluxes for the corresponding light curves.

6. OBLIQUITY MODEL RESULTS

We start by examining runs where the rotation rate is fixed to the sub-synchronous value, as defined in Equation 10. Our initial best-fit models prefer nearly orthogonal spin-orbit alignments ($\psi \approx 90^\circ$) for both planets in $3.6\text{ }\mu\text{m}$, and for WASP-12 b in $4.5\text{ }\mu\text{m}$ (Table 2). We note that the best-fit radiative timescales for HD 149026 b in $4.5\text{ }\mu\text{m}$, and especially so for WASP-12 b at $3.6\text{ }\mu\text{m}$, are short and therefore much less sensitive to the spin rate and geometry. Figures 6–7 show the best-fit light curves in each band, and corresponding orientations of the planets’ axes as would be seen from our line of sight.

There are also (old) results from the freely-varying rotation rate runs in the table, but I don’t trust them and am re-running MCMC chains with the latest version of the model. I should also re-run the models where the obliquities vary together. When we have up-to-date results, this is where they go!

7. DISCUSSION

While most thermal light curves of close-in giant planets demonstrate eastward phase offsets, consistent with super-rotating winds, there are now at least two planets with significant observed westward offsets. We have demonstrated that one way of producing westward offsets is to consider variations in the spin axis orientation, which fundamentally changes the relationship between

the instellation variations due to the rotation and those due to the orbit. Planets on very short orbits occupy a particularly interesting regime where we may reasonably expect the rotation and orbital rates to be comparable; therefore changes in the spin geometry can have major effects on observed phases.

Our dynamical arguments point to a range of parameter space where an unseen outer planet, particularly in the case of the HD 149026 system, could be in a position to induce a spin-orbit resonance with HD 149026 b. Such results leave open the possibility that HD 149026 b may be locked into a stable, high-obliquity spin state, thereby warranting a consideration of oblique models in explaining the observed phase photometry.

We apply thermal models to two planets, HD 149026 b and WASP-12 b, allowing the spin orientation to vary freely. A combination of sufficiently long thermal timescales and spin axes nearly perpendicular to the orbit normal can reproduce the strong westward offset in the $3.6\text{ }\mu\text{m}$ data of HD 149026 b. However, for WASP-12 b, variations near quadrature cannot be effectively reproduced for a simple thermal model with free spin geometry, suggesting either that more complex tidal distortion models, or refined instrumental characterization, need to be considered to help explain these phase curves.

We have also not considered the degeneracies inherent to a modeling approach that considers only the output 1-D photometry. Many advances have been made recently that focus on first constructing physical 2- or 3-dimensional maps of the planetary flux, then calculating photometric variations (e.g. [Rauscher et al. 2018](#)). These will very likely be the most rigorous frameworks for modeling photometry in the future. Despite these limitations, and acknowledging that there are multiple potential explanations for westward offsets, we have shown that, to first order, highly-oblique Hot Jupiters should have different morphologies from those with little to no obliquity.

APPENDIX

A. ESTIMATING PHASE OFFSETS IN A WORLD WITH OBLIQUITY

In the simple case of non-oblique rotation, it is fairly straightforward to estimate a phase offset from geometry alone (see e.g. §4, and in particular Equation 3, in [Cowan et al. 2012b](#)). If one also assumes a circular orbit, then the convolution of the viewing geometry does not add any significant challenges. In the more general case of oblique and potentially eccentric planets, estimating the predicted geometric phase offset requires a careful treatment of the instellation and viewing angles. To start, we may re-express Equation 18 in the rotating frame, with planet-centric longitude ϕ and latitude θ , as

$$\begin{aligned} \cos \alpha_\star &= \cos [(\phi + \omega_{\text{rot}} t) - (\nu - \zeta)] \times \\ &\quad \cos [\theta + \psi \cos (\nu - \zeta)] \end{aligned} \tag{A1}$$

Table 2. Best-Fit Parameters from Radiative Model

	HD 149026 b		WASP-12 b		CoRoT-2 b
Parameter	3.6 μm	4.5 μm	3.6 μm	4.5 μm	4.5 μm
Sub-synchronous Rotation					
τ_{rad} (hr)	$7.7^{+10.8}_{-4.6}$	$2.4^{+24.0}_{-1.3}$	$0.01^{+0.01}_{-0.01}$	$65.5^{+24.3}_{-0.3}$	$23.9^{+2.5}_{-3.1}$
T_0 (K)	877^{+388}_{-631}	1388^{+155}_{-158}	$427^{+166}_{-N/A}$	2458^{+84}_{-141}	92^{+209}_{-52}
A	< 0.12	$0.64^{+0.09}_{-0.05}$	< 0.06	$0.36^{+0.09}_{-0.35}$	< 0.03
ψ ($^\circ$)	$93.9^{+45.1}_{-32.5}$	$4.2^{+47.7}_{-1.9}$	$87.9^{+0.6}_{-8.5}$	$91.2^{+70.1}_{-3.1}$	45.8 ± 1.4
ζ ($^\circ$)	$10.6^{+143.7}_{-170.42}$	$-29.0^{+113.0}_{-149.2}$	$-39.4^{+4.4}_{-0.9}$	$-73.0^{+21.2}_{-58.6}$	$-82.5^{+10.8}_{-7.1}$
Free Rotation					
$P_{\text{rot}}/P_{\text{orb}}$	$0.29^{+0.30}_{-0.09}$	$0.18^{+0.51}_{-0.03}$	$0.77^{+0.14}_{-0.04}$	0.94 ± 0.01	
τ_{rad} (hr)	$14.4^{+31.9}_{-3.6}$	$11.1^{+10.4}_{-4.4}$	$12.7^{+32.2}_{-2.7}$	$40.0^{+8.1}_{-3.4}$	
T_0 (K)	697^{+476}_{-288}	1211^{+336}_{-433}	1567^{+134}_{-63}	2204^{+40}_{-14}	
A	$0.07^{+0.10}_{-0.05}$	$0.37^{+0.28}_{-0.08}$	$0.09^{+0.02}_{-0.08}$	< 0.03	
ψ ($^\circ$)	$0.5^{+54.2}_{-0.3}$	$104.2^{+36.3}_{-56.7}$	$0.8^{+6.0}_{-0.4}$	$21.1^{+8.5}_{-10.1}$	
ζ ($^\circ$)	$-5.1^{+99.6}_{-131.04}$	$60.3^{+36.6}_{-35.9}$	$-67.0^{+123.4}_{-N/A}$	$46.6^{+58.3}_{-12.1}$	

NOTE—The parameter values from our blackbody model returning the most favorable likelihood from MCMC algorithms. Uncertainties listed are 1- σ ranges of a Metropolis-Hastings algorithm walk around the region of most favorable likelihood in parameter space. Upper limits imply the best-fit values are zero, with a 1- σ uncertainty given by the upper limit.

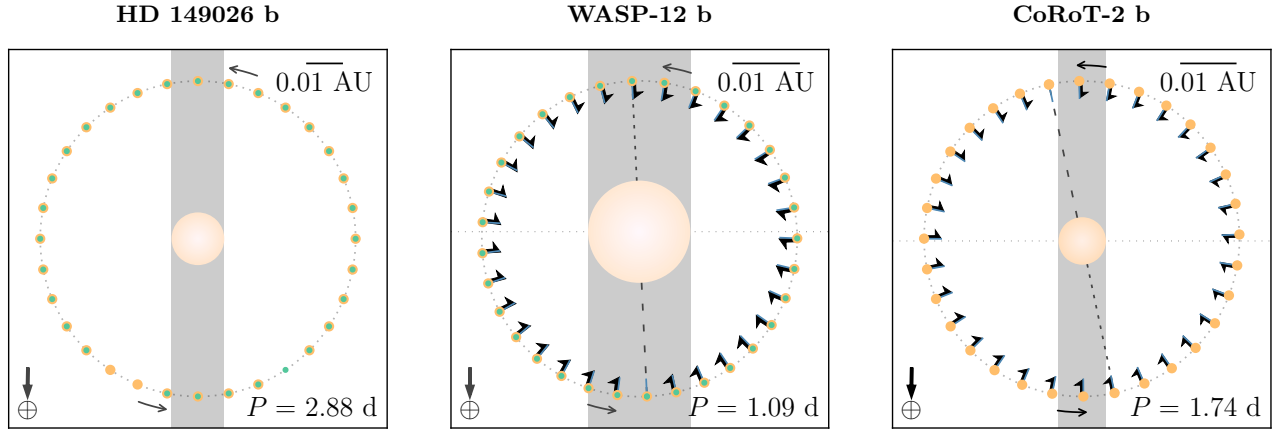


Figure 5. Top-down orbital diagrams of HD 149026 b (left), WASP-12 b (center), and CoRoT-2 b (right). The stars are drawn to scale with respect to the orbits, and the concentric colored rings show a binned coverage of each phase curve, with 3.6 μm in green and 4.5 μm in yellow.

where in the circular limit, $\nu \rightarrow \bar{\omega}_{\text{orb}} t$, for $\bar{\omega}_{\text{orb}} \equiv 2\pi/P_{\text{orb}}$. We can write a similar attenuation factor $\cos \alpha_{\text{obs}} \equiv \hat{n} \cdot \hat{r}_{\text{obs}}$, for planet surface normal \hat{n} and line-of-sight direction \hat{r}_{obs} , with

$$\cos \alpha_{\text{obs}} = \cos [(\phi + \omega_{\text{rot}} t) - (\nu_{\text{tr}} - \zeta)] \times \cos [\theta + \psi \cos (\nu_{\text{tr}} - \zeta)] \quad (\text{A2})$$

where $\nu_{\text{tr}} \equiv \pi/2 - \varpi$ is the true anomaly during transit.

In the regime where the radiative timescale is shorter than the characteristic timescales of the sub-stellar motion (i.e. the rotation and orbital periods) we can treat the thermal emission as periodic with respect to the instellation, but

HD 149026 b

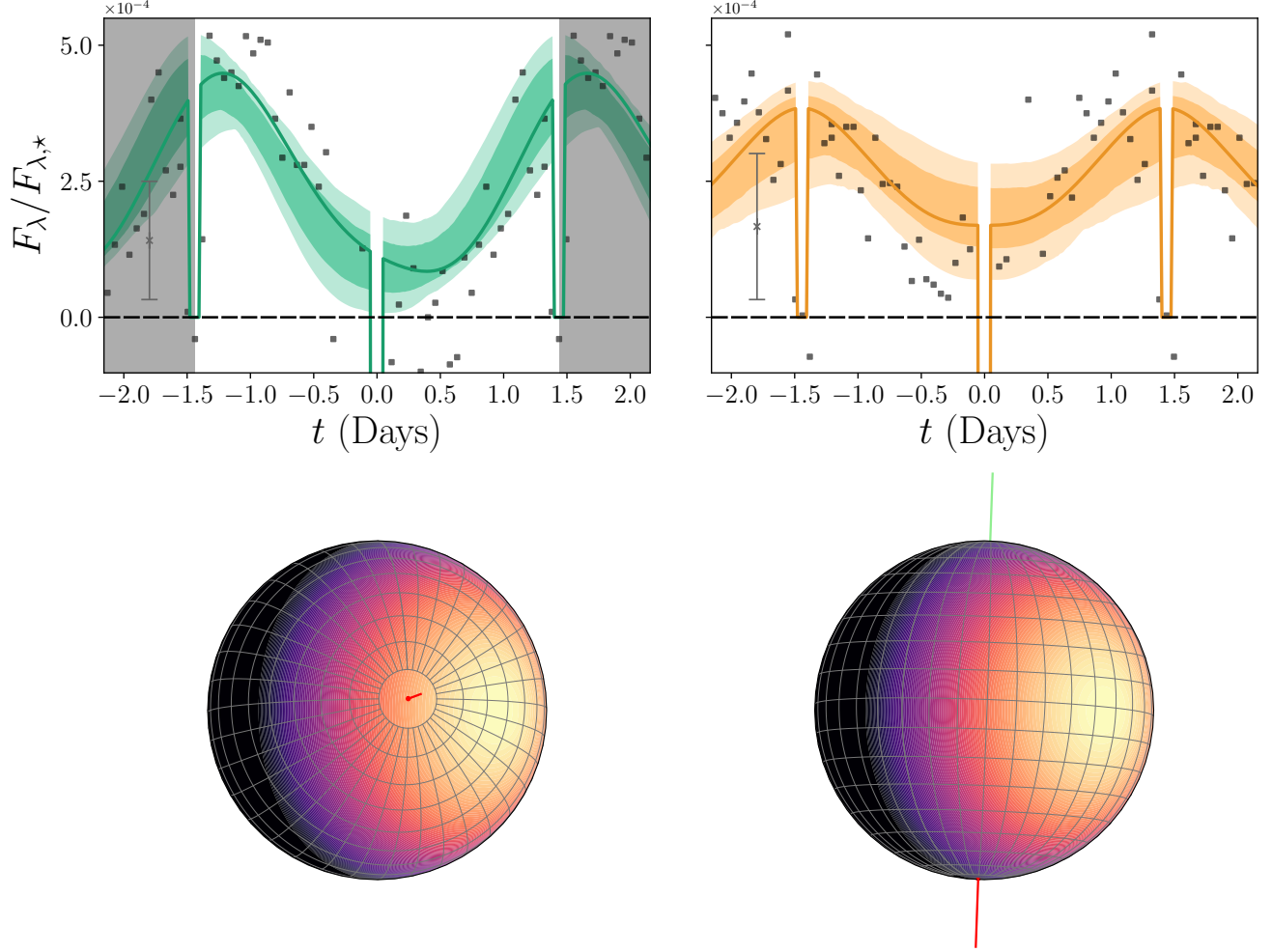


Figure 6. *Top:* the best-fit oblique thermal models for HD 149026 b, in the 3.6 (left) and 4.5 (right) μm channels. The colored lines represent the best-fit light curve, with the shaded regions representing the 1- and 2- σ uncertainty bounds (darker and lighter, respectively). The black points represent the binned data from [Zhang et al. \(2018\)](#). *Bottom:* globes showing the best-fit orientation of the spin axes for each band, as viewed along our line of sight.

with a temporal lag given by a thermal timescale τ_{thm} . This timescale ultimately relates to, but may not necessarily be, the radiative timescale. Therefore we construct a thermal attenuation

$$\begin{aligned} \cos \alpha_{\text{thm}} &\equiv \cos \alpha_{\star}(t - \tau_{\text{thm}}) \\ &\cos \{ [\phi + \omega_{\text{rot}}(t - \tau_{\text{thm}})] - (\nu(t - \tau_{\text{thm}}) - \zeta) \} \times \\ &\cos \{ \theta + \psi \cos [\nu(t - \tau_{\text{thm}}) - \zeta] \}. \end{aligned} \quad (\text{A3})$$

Our approach considers the evolution of this thermal attenuation at the sub-observer point, whose planet-centric coordinates are

$$\begin{aligned} \phi &= -[\omega_{\text{rot}}t - (\nu_{\text{tr}} - \zeta)] \\ \theta &= -\psi \cos(\nu_{\text{tr}} - \zeta), \end{aligned} \quad (\text{A4})$$

WASP-12 b

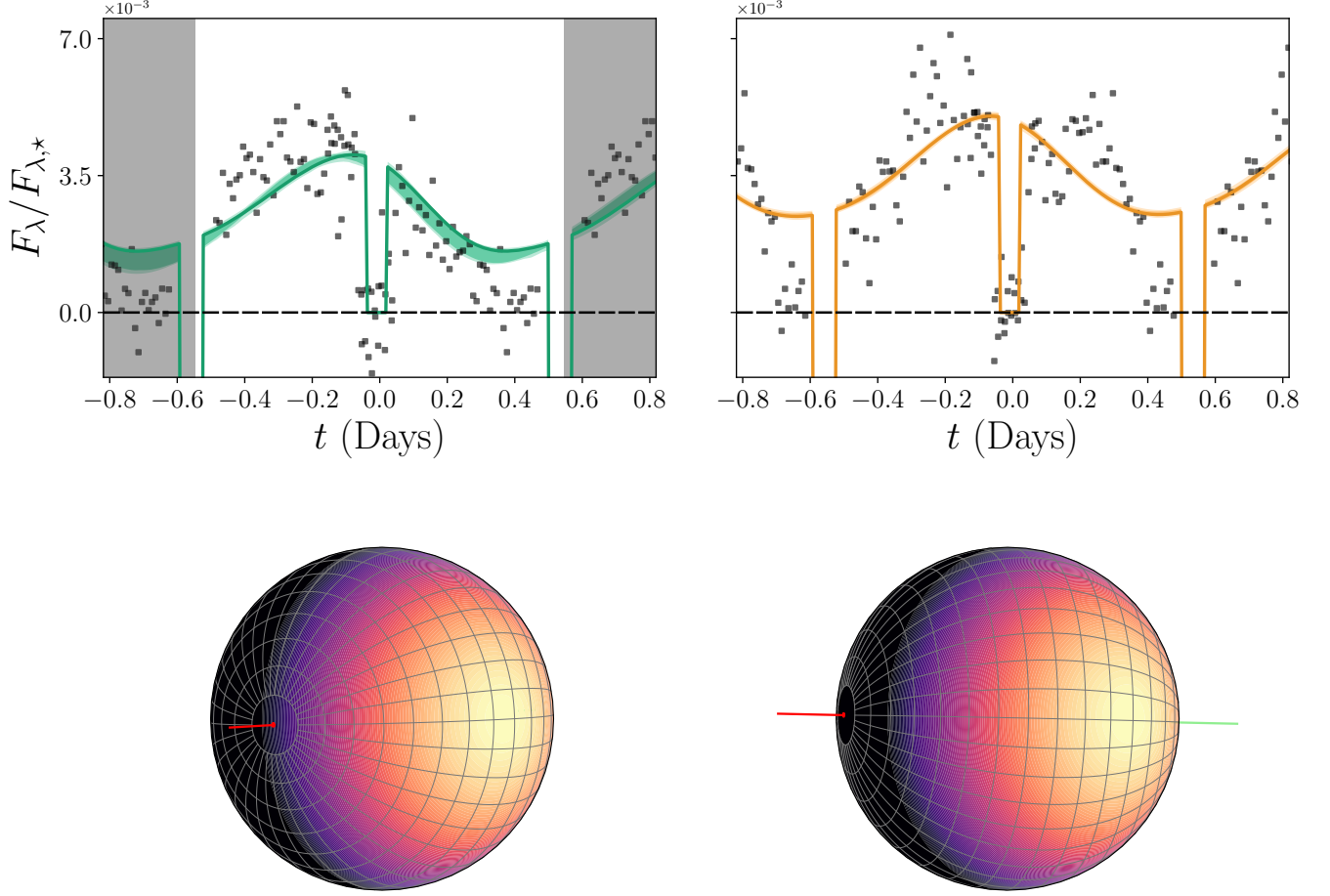


Figure 7. *Top:* the best-fit oblique thermal models for WASP-12 b, in the 3.6 (left) and 4.5 (right) μm channels. The colored lines represent the best-fit light curve, with the shaded regions representing the 1- and 2- σ uncertainty bounds (darker and lighter, respectively). The black points represent the binned data from Cowan et al. (2012a). *Bottom:* globes showing the best-fit orientation of the spin axes for each band, as viewed along our line of sight.

and solve for the positions in anomaly where $d(\cos \alpha_{\text{thm}})/dt$ at this point goes to zero. From this we determine that such orbital positions should satisfy the following condition:

$$\tan[\omega_{\text{rot}}\tau_{\text{thm}} + (\nu' - \nu'_{\text{tr}})] + \psi \sin \nu' \tan[\psi (\cos \nu' + \cos \nu'_{\text{tr}})] = 0 \quad (\text{A5})$$

where $\nu' \equiv \nu(t - \tau_{\text{thm}}) - \zeta$ and $\nu'_{\text{tr}} \equiv \nu_{\text{tr}} - \zeta$. Note that this formulation is unchanged if we add a multiple of π to ζ . This reflects the symmetry that the observed brightness will look the same regardless of which hemisphere is experiencing which season at any given time.

This material is based upon work supported by the National Aeronautics and Space Administration through the NASA Astrobiology Institute under Cooperative Agreement Notice NNN13ZDA017C issued through the Science Mission Directorate. We acknowledge support from the NASA Astrobiology Institute through a cooperative agreement between NASA Ames Research Center and Yale University.

This research has made use of the NASA Exoplanet Archive, which is operated by the California Institute of Technology, under contract with the National Aeronautics and Space Administration under the Exoplanet Exploration Program.

Facility: Exoplanet Archive, Kepler, Spitzer (IRAC)

Software: Astropy (Astropy Collaboration et al. 2013), Colorcet (Kovesi 2015), Jupyter (Kluyver et al. 2016), Matplotlib (Hunter 2007), Numpy (van der Walt et al. 2011), Paletton (Staníček 2018), Scipy (Jones et al. 2001), WebPlotDigitizer (Rohatgi 2017)

REFERENCES

- Adams, A. D., & Laughlin, G. 2018, *Astron. J.*, 156, 28, doi: [10.3847/1538-3881/aac437](https://doi.org/10.3847/1538-3881/aac437)
- Astropy Collaboration, Robitaille, T., Tollerud, E., et al. 2013, *A&A*, 558, A33, doi: [10.1051/0004-6361/201322068](https://doi.org/10.1051/0004-6361/201322068)
- Bailey, A., & Goodman, J. 2018, 12, 1, <https://arxiv.org/abs/1808.00052>
- Broeg, C., & Wuchterl, G. 2007, *Mon. Not. R. Astron. Soc. Lett.*, 376, L62, doi: [10.1111/j.1745-3933.2007.00287.x](https://doi.org/10.1111/j.1745-3933.2007.00287.x)
- Brown, D. J. A., Cameron, A. C., Hall, C., Hebb, L., & Smalley, B. 2011, *Mon. Not. R. Astron. Soc.*, 415, 605, doi: [10.1111/j.1365-2966.2011.18729.x](https://doi.org/10.1111/j.1365-2966.2011.18729.x)
- Burrows, A., Hubeny, I., Budaj, J., & Hubbard, W. B. 2007, *Astrophys. J.*, 661, 502, doi: [10.1086/514326](https://doi.org/10.1086/514326)
- Butler, R. P., Vogt, S. S., Laughlin, G., et al. 2017, *Astron. J.*, 153, 208, doi: [10.3847/1538-3881/aa66ca](https://doi.org/10.3847/1538-3881/aa66ca)
- Campo, C. J., Harrington, J., Hardy, R. A., et al. 2011, *Astrophys. J.*, 727, 125, doi: [10.1088/0004-637X/727/2/125](https://doi.org/10.1088/0004-637X/727/2/125)
- Carter, J., Winn, J., Gilliland, R., & Holman, M. 2009, *ApJ*, 696, 241, doi: [10.1088/0004-637X/696/1/241](https://doi.org/10.1088/0004-637X/696/1/241)
- Chan, T., Ingemyr, M., Winn, J. N., et al. 2012, *Astron. J.*, 144, 90
- Charbonneau, D., Winn, J. N., Latham, D. W., et al. 2006, *Astrophys. J.*, 636, 445, doi: [10.1086/497959](https://doi.org/10.1086/497959)
- Colombo, G. 1966, *AJ*, 71, 1, doi: [10.1007/s13398-014-0173-7.2](https://doi.org/10.1007/s13398-014-0173-7.2)
- Cowan, N., & Agol, E. 2011, *ApJ*, 726, 82, doi: [10.1088/0004-637X/726/2/82](https://doi.org/10.1088/0004-637X/726/2/82)
- Cowan, N., Machalek, P., Croll, B., et al. 2012a, *ApJ*, 747, 82, doi: [10.1088/0004-637X/747/1/82](https://doi.org/10.1088/0004-637X/747/1/82)
- Cowan, N. B., Voigt, A., & Abbot, D. S. 2012b, *Astrophys. J.*, 757, doi: [10.1088/0004-637X/757/1/80](https://doi.org/10.1088/0004-637X/757/1/80)
- Croll, B., Lafreniere, D., Albert, L., et al. 2011, *AJ*, 141, 30, doi: [10.1088/0004-6256/141/2/30](https://doi.org/10.1088/0004-6256/141/2/30)
- de Wit, J., Lewis, N., Langton, J., et al. 2016, *ApJL*, 820, L33, doi: [10.3847/2041-8205/820/2/L33](https://doi.org/10.3847/2041-8205/820/2/L33)
- Debrecht, A., Carroll-Nellenback, J., Frank, A., et al. 2018, 8, 1, doi: [10.1093/mnras/sty1164](https://doi.org/10.1093/mnras/sty1164)
- Fabrycky, D. C., Johnson, E. T., & Goodman, J. 2007, *Astrophys. J.*, 665, 754, doi: [10.1086/519075](https://doi.org/10.1086/519075)
- Farr, B., Farr, W. M., Cowan, N. B., Haggard, H. M., & Robinson, T. 2018, 0, <https://arxiv.org/abs/1802.06805v1>
- Fortney, J. J., Saumon, D., Marley, M. S., Lodders, K., & Freedman, R. S. 2006, *Astrophys. J.*, 642, 495, doi: [10.1086/500920](https://doi.org/10.1086/500920)
- Fossati, L., Ayres, T. R., Haswell, C. A., et al. 2013, *Astrophys. J.*, 766, L20, doi: [10.1088/2041-8205/766/2/L20](https://doi.org/10.1088/2041-8205/766/2/L20)
- Fossati, L., Haswell, C. A., Froning, C. S., et al. 2010, *Astrophys. J.*, 714, L222, doi: [10.1088/2041-8205/714/2/L222](https://doi.org/10.1088/2041-8205/714/2/L222)
- Fujii, Y., & Kawahara, H. 2012, *Astrophys. J.*, 755, doi: [10.1088/0004-637X/755/2/101](https://doi.org/10.1088/0004-637X/755/2/101)
- Gladman, B., Quinn, D. D., Nicholson, P., & Rand, R. 1996, *Icarus*, 122, 166, doi: [10.1006/icar.1996.0117](https://doi.org/10.1006/icar.1996.0117)
- Hamilton, D. P., & Ward, W. R. 2004, *Astron. J.*, 128, 2510, doi: [10.1086/424534](https://doi.org/10.1086/424534)
- Han, E., Wang, S., Wright, J., et al. 2014, *PASP*, 126, 827, doi: [10.1086/678447](https://doi.org/10.1086/678447)
- Haswell, C. A., Fossati, L., Ayres, T., et al. 2012, *Astrophys. J.*, 760, doi: [10.1088/0004-637X/760/1/79](https://doi.org/10.1088/0004-637X/760/1/79)
- Hebb, L., Collier-Cameron, A., Loeillet, B., et al. 2009, *Astrophys. J.*, 693, 1920, doi: [10.1088/0004-637X/693/2/1920](https://doi.org/10.1088/0004-637X/693/2/1920)
- Hunter, J. D. 2007, *Comput. Sci. Eng.*, 9, 90, doi: [10.1109/MCSE.2007.55](https://doi.org/10.1109/MCSE.2007.55)
- Hut, P. 1981, *A&A*, 99, 126
- Ikoma, M., Guillot, T., Genda, H., Tanigawa, T., & Ida, S. 2006, *Astrophys. J.*, 650, 1150, doi: [10.1086/507088](https://doi.org/10.1086/507088)
- Jones, E., Oliphant, T., Peterson, P., & Others. 2001, *SciPy: Open source scientific tools for Python.* <http://www.scipy.org/>
- Kawahara, H. 2016, *Astrophys. J.*, 822, 1, doi: [10.3847/0004-637X/822/2/112](https://doi.org/10.3847/0004-637X/822/2/112)
- Kawahara, H., & Fujii, Y. 2010, *Astrophys. J.*, 720, 1333, doi: [10.1088/0004-637X/720/2/1333](https://doi.org/10.1088/0004-637X/720/2/1333)

- . 2011, *Astrophys. J. Lett.*, 739, 2, doi: [10.1088/2041-8205/739/2/L62](https://doi.org/10.1088/2041-8205/739/2/L62)
- Kluyver, T., Ragan-Kelley, B., Perez, F., et al. 2016, IOS Press, 87
- Knutson, H., Charbonneau, D., Cowan, N., et al. 2009a, *ApJ*, 690, 822, doi: [10.1088/0004-637X/690/1/822](https://doi.org/10.1088/0004-637X/690/1/822)
- Knutson, H., Lewis, N., Fortney, J., et al. 2012, *ApJ*, 754, 22, doi: [10.1088/0004-637X/754/1/22](https://doi.org/10.1088/0004-637X/754/1/22)
- Knutson, H. A., Charbonneau, D., Cowan, N. B., et al. 2009b, *Astrophys. J.*, 703, 769
- Knutson, H. A., Charbonneau, D., Allen, L. E., et al. 2007, *Nature*, 447, 183, doi: [10.1038/nature05782](https://doi.org/10.1038/nature05782)
- Kovesi, P. 2015, ArXiv e-prints, <https://arxiv.org/abs/1509.03700>
- Kramm, U., Nettelmann, N., Redmer, R., & Stevenson, D. J. 2011, *Astron. Astrophys.*, 528, A18, doi: [10.1051/0004-6361/201015803](https://doi.org/10.1051/0004-6361/201015803)
- Lai, D., Helling, C., & van den Heuvel, E. 2010, *ApJ*, 721, 923, doi: [10.1088/0004-637X/721/2/923](https://doi.org/10.1088/0004-637X/721/2/923)
- Laughlin, G., Deming, D., Langton, J., et al. 2009, *Nature*, 457, 562, doi: [10.1038/nature07649](https://doi.org/10.1038/nature07649)
- Levrard, B., Correia, A. C. M., Chabrier, G., et al. 2007, *Astron. Astrophys.*, 462, L5, doi: [10.1051/0004-6361:20066487](https://doi.org/10.1051/0004-6361:20066487)
- Li, S.-L., Miller, N., Lin, D., & Fortney, J. 2010, *Nature*, 463, 1054, doi: [10.1038/nature08715](https://doi.org/10.1038/nature08715)
- Maciejewski, G., Errmann, R., Raetz, S., et al. 2011, *Astron. Astrophys.*, 528, A65, doi: [10.1051/0004-6361/201016268](https://doi.org/10.1051/0004-6361/201016268)
- Maciejewski, G., Dimitrov, D., Fernández, M., et al. 2016, *Astron. Astrophys.*, 588, L6, doi: [10.1051/0004-6361/201628312](https://doi.org/10.1051/0004-6361/201628312)
- Mandell, A. M., Haynes, K., Sinukoff, E., et al. 2013, *Astrophys. J.*, 779, 128, doi: [10.1088/0004-637X/779/2/128](https://doi.org/10.1088/0004-637X/779/2/128)
- Murray, C., & Dermott, S. 1999, *Solar system dynamics*
- Nutzman, P., Charbonneau, D., Winn, J. N., et al. 2009, *Astrophys. J.*, 692, 229
- Peale, S. J. 1969, *Astron. J.*, 74, 483, doi: [10.1086/110825](https://doi.org/10.1086/110825)
- . 2006, *Icarus*, 181, 338, doi: [10.1016/j.icarus.2005.10.006](https://doi.org/10.1016/j.icarus.2005.10.006)
- Ragozzine, D., & Wolf, A. S. 2009, *Astrophys. J.*, 698, 1778, doi: [10.1088/0004-637X/698/2/1778](https://doi.org/10.1088/0004-637X/698/2/1778)
- Rauscher, E., Suri, V., & Cowan, N. B. 2018, <https://arxiv.org/abs/1806.05700>
- Rein, H., & Liu, S.-F. 2012, *Astron. Astrophys.*, 537, A128, doi: [10.1051/0004-6361/201118085](https://doi.org/10.1051/0004-6361/201118085)
- Rein, H., & Spiegel, D. S. 2015, *Mon. Not. R. Astron. Soc.*, 446, 1424, doi: [10.1093/mnras/stu2164](https://doi.org/10.1093/mnras/stu2164)
- Rodríguez, A., & Ferraz-Mello, S. 2010, *EAS Publ. Ser.*, 42, 411, doi: [10.1051/eas/1042044](https://doi.org/10.1051/eas/1042044)
- Rohatgi, A. 2017, WebPlotDigitizer, <https://automeris.io/WebPlotDigitizer>
- Rowe, J. F., Bryson, S. T., Marcy, G. W., et al. 2014, *Astrophys. J.*, 784, 45, doi: [10.1088/0004-637X/784/1/45](https://doi.org/10.1088/0004-637X/784/1/45)
- Sato, B., Fischer, D. A., Henry, G. W., et al. 2005, *Astrophys. J.*, 633, 465, doi: [10.1086/449306](https://doi.org/10.1086/449306)
- Schwartz, J. C., Sekowski, C., Haggard, H. M., Pallé, E., & Cowan, N. B. 2016, *Mon. Not. R. Astron. Soc.*, 457, 926, doi: [10.1093/mnras/stw068](https://doi.org/10.1093/mnras/stw068)
- Schwartz, J. J. C., Kashner, Z., Jovmir, D., & Cowan, N. B. 2017, ArXiv e-prints, doi: [10.3847/1538-4357/aa9567](https://doi.org/10.3847/1538-4357/aa9567)
- Shporer, A. 2017, *PASP*, 129, 72001, doi: [10.1088/1538-3873/aa7112](https://doi.org/10.1088/1538-3873/aa7112)
- Staníček, P. 2018, Paletton, the color scheme designer, <http://paletton.com/>
- Stassun, K. G., Collins, K. A., & Gaudi, B. S. 2017, *Astron. J.*, 153, 136, doi: [10.3847/1538-3881/aa5df3](https://doi.org/10.3847/1538-3881/aa5df3)
- Stevenson, K., Bean, J., Madhusudhan, N., & Harrington, J. 2014, *ApJ*, 791, 36, doi: [10.1088/0004-637X/791/1/36](https://doi.org/10.1088/0004-637X/791/1/36)
- Stevenson, K. B., Harrington, J., Fortney, J. J., et al. 2012, *Astrophys. J.*, 754, 136, doi: [10.1088/0004-637X/754/2/136](https://doi.org/10.1088/0004-637X/754/2/136)
- van der Walt, S., Colbert, S. C., & Varoquaux, G. 2011, *Comput. Sci. Eng.*, 13, 22, doi: [10.1109/MCSE.2011.37](https://doi.org/10.1109/MCSE.2011.37)
- Van Eylen, V., & Albrecht, S. 2015, *Astrophys. J.*, 808, 126, doi: [10.1088/0004-637X/808/2/126](https://doi.org/10.1088/0004-637X/808/2/126)
- Ward, W. R. 1975, *Astron. J.*, 80, 64, doi: [10.1086/111714](https://doi.org/10.1086/111714)
- Ward, W. R., & Hamilton, D. P. 2004, *Astron. J.*, 128, 2501, doi: [10.1086/424533](https://doi.org/10.1086/424533)
- Winn, J. N., Henry, G. W., Torres, G., & Holman, M. J. 2008, *Astrophys. J.*, 675, 1531, doi: [10.1086/527032](https://doi.org/10.1086/527032)
- Wolf, A. S., Laughlin, G., Henry, G. W., et al. 2007, *Astrophys. J.*, 667, 549, doi: [10.1086/503354](https://doi.org/10.1086/503354)
- Zellem, R., Lewis, N., Knutson, H., et al. 2014, *ApJ*, 790, 53, doi: [10.1088/0004-637X/790/1/53](https://doi.org/10.1088/0004-637X/790/1/53)
- Zhang, M., Knutson, H. A., Kataria, T., et al. 2018, *Astron. J.*, 155, 83, doi: [10.3847/1538-3881/aaa458](https://doi.org/10.3847/1538-3881/aaa458)